Local earthquake tomography of the Altiplano and the Eastern Cordillera of northern Bolivia

Catherine Dorbath [a,b,*], Michel Granet [a]

[a] ORSTOM, 213 rue la Fayette, 75480 Paris Cedex 10, France
[b] EOPGS, 5 rue René Descartes, 67084 Strasbourg Cedex, France

Abstract

The velocity structure in the crust beneath the central Andes of northern Bolivia is obtained by the simultaneous inversion of local earthquake arrival-time data for velocity and hypocentral parameters. The data were recorded between October 1990 and February 1991 by the French "Lithoscope" network; the 34 vertical, short-period seismic stations were installed along a 320-km-long profile crossing two main morphological units of the Andean chain; the Altiplano and the Eastern Cordillera. The arrival times of seismic waves generated by earthquakes located in the subduction zone of the Nazca plate underneath the South American plate were inverted using a modified version of Thurber's 3-D iterative simultaneous inversion code.

The results are consistent with the inversion of teleseismic travel-time residuals from the same network and closely correlate with the mapped surface geological features. The Altiplano Basin is characterized by a low-velocity zone down to 20 km, enclosed by the San Andres and Laurani faults. At the surface, the Cordillera Real fault zone (CRFZ) bounds to the west the high P-wave velocity anomaly lying under the axial zone of the Eastern Cordillera. The velocity discontinuity dips steeply to the southwest, to the bottom of the crust. From the velocity model, the depth of the Moho is estimated to be 66 km under the Altiplano. Moreover, the different behaviour of P- and S-waves found below the Western Cordillera and above the slab is consistent with the presence of partially melted asthenosphere that may be responsible for the magmatic activity. Finally, the seismicity defines, between 90 and 225 km, a part of the slab dipping to the north-northeast with a low angle of about 30°.

1. Introduction

This paper describes the results of inverting arrival times of seismic waves generated by earthquakes located in the Nazca plate subduction zone recorded by a local seismic network, first to determine the velocity structures in northern Bolivia above the subduction zone and, second, to improve the location of these earthquakes to examine the geometry of the subducted slab.

Between October 1990 and February 1991, a seismic field experiment was carried out in northern Bolivia. Thirty-four vertical short-period seismic stations of the French "Lithoscope" network were installed along a 320-km-long profile, with a mean station spacing of 10 km (Fig. 1). This seismic profile was located across the NW–SW-oriented seg-

---
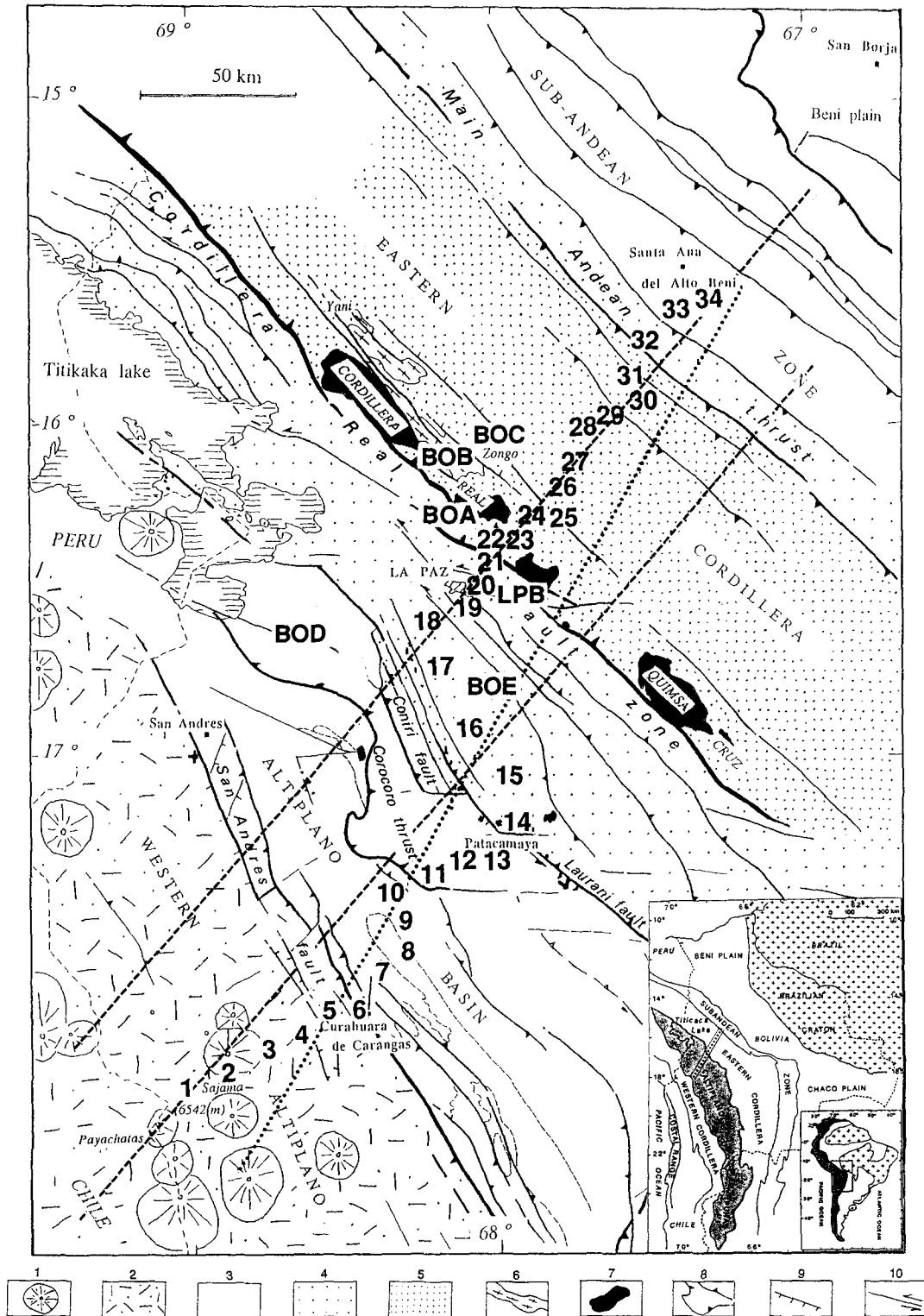
ment of the Andean Cordillera, just north of the latitude where the chain changes its trend from the NW–SW direction to an overall N–S direction in the south. The profile extended from the Volcanic arc, on the Chilean border, to the sub-Andean zone, near to the Rio Beni. Thus, it crossed two main morphological units of the Andean chain, the Altiplano and the Eastern Cordillera, in a direction approximately perpendicular to the structural trend of the Andean chain.

The structural zones of the Andean Belt roughly correspond to the morphological units. The Altiplano domain (4000 m high) is limited by the volcanic arc to the west and the Eastern Cordillera to the east. In the northern part of the Bolivian Altiplano, the longitudinal "San Andres fault zone" separates the volcanic western Altiplano (stations 1–5, Fig. 1) from the central Altiplano (stations 7–13, Fig. 1), a Tertiary intracordilleran Basin which subsided during Cenozoic times (Martinez, 1980; Dalmayrac et al., 1980). Along the zone of the profile, the Cenozoic continental detrital series, which was deposited in a compressional shortening regime, is more than 10 km thick (Martinez and Seguret, 1990). The limit between the basin and the thick Paleozoic series of the western flank of the Eastern Cordillera is marked by the "Coniri–Laurani fault zone". The western flank (stations 15–20, Fig. 1) extends to the east up to the Cordillera Real fault zone (CRFZ) (stations 21–23, Fig. 1) which corresponds to steeply dipping NW–SE-trending reverse faults with a left-lateral strike-slip component (Martinez, 1980; Lavenu, 1986). The axial zone of the Cordillera (stations 24–31, Fig. 1) is mainly formed by outcrops of Ordovician series, folded and metamorphosed during Hercynian times and intruded, close to the CRFZ, by

Hercynian to Andean plutons. On the northeastern flank of the axial zone, large longitudinal faults [Main Andean Thrust (MAT), Roeder (1988)] mark the transition into the sub-Andean zone whose Paleozoic and Mesozoic series is probably over 10 km thick (stations 32–34, Fig. 1).

During the field experiment we recorded about 500 events. Among them, less than a hundred were reported in the NEIC monthly listings: 85 were distant earthquakes, eleven were local events. P-teleseismic delay times were inverted to study the lithosphere and map relative velocity perturbations beneath the Altiplano and the Eastern Cordillera down to 150 km. The results of the teleseismic study have been published in a previous paper (Dorbath et al., 1993) as well as a precise description of the structural setting of central Andes and a review of previous geophysical work.

Although bulletins reported very few local events, a careful examination of the seismic signals indicated that most of the remaining events were actually local earthquakes whose magnitude did not allow location by NEIC. Therefore, we exploit these data by running a simultaneous inversion of hypocenters and velocity.

Aki and Lee (1976) first demonstrated the usefulness of this method studying the San Andreas fault. Thurber (1983) developed an iterative inversion technique that included an approximate 3-D ray-tracing routine. More recently, Eberhart-Phillips (1989, 1990) has extended Thurber's method to include S-wave velocity. Compared to teleseismic tomography, local earthquake tomography (LET) can usually offer a much higher spatial resolution of structure due to the increased density of ray sampling and the higher frequency content of local signals. On the

Fig. 1. Geological setting of the region under study after Martinez (Dorbath et al., 1993). The numbers of the legend refer to the different geological and tectonic units: *1* = Quaternary volcanoes; *2* = Cenozoic volcano-sedimentary cover; *3* = Meso-Cenozoic Altiplano Basin and Paleozoic–Mesozoic–Cenozoic sub-Andes; *4* = Siluro-Devonian borders of the Eastern Cordillera; *5* = Ordovician axial zone of the Eastern Cordillera; *6* = Hercynian plutons; *7* = Andean plutons; *8* = thrust fault; *9* = normal fault; *10* = strike-slip fault. The bold numbers show the location of the temporary seismic stations; the permanent Bolivian stations are represented by their code names. The dotted line shows the location of the cross section for the teleseismic inversion model presented in Fig. 8c. The dashed lines show the locations of the northern and southern cross sections through the local earthquake inversion model. The insert shows the morphostructural zoning of the Central Andes. From the Pacific Ocean to the Brazilian craton (area marked with crosses), the main units are: the Coastal Range, the Axial Valley, the Western Cordillera, the Altiplano–Puna region (shaded area), the Eastern Cordillera and the sub-Andean zone. Crossing the Altiplano and the Eastern Cordillera, between 15 and 18°S and 67 and 69°W, the dotted line shows the approximate location of the teleseismic study described in this paper. The rectangle in the insert shows the location of the Central Andes in South America.

other hand, the depth extent of LET models will be limited by the maximum earthquake focal depths in the area.

The possibility offered by LET to get velocity structures and not simply perturbations of the velocity is very useful in order to improve the knowledge of geological units and also in estimating the Moho depths. Another objective is to compare the LET result, in terms of P-wave velocity perturbations, to the model obtained by the teleseismic inversion. Moreover, the comparison between P- and S-wave velocity models provides information about the medium rheology.

2. Data selection

The data used in this study are arrival times of compressional P-waves and shear S-waves from local earthquakes recorded by the temporary network together with the stations from the permanent Bolivian network located within the same area. The 34 temporary digital recorders of the French "Lithoscope" network were equipped with vertical short-period seismometers (Mark Product L4C, $T_0 = 1$ s). They were installed accross the Altiplano and the Eastern Cordillera perpendicular to the trend of the main Andean structures (N320°E), which show an

Table 1
Temporary stations coordinates

No.	Name	Code	Latitude (°S)	Longitude (°W)	Altitude (m)
1	Mujtalla	MUJT	−18.0581	−68.9656	4338
2	Caripe	CARI	−18.0032	−68.8408	4230
3	Tolatia	TOLA	−17.9388	−68.7384	4077
4	Catacora	CATA	−17.9135	−68.6169	3920
5	Kelkata	KELK	−17.8436	−68.5331	3900
6	Curahuara	CURA	−17.8261	−68.4269	3912
7	Bella Vista	BEVI	−17.7208	−68.3715	3901
8	Posotalla	POSO	−17.6435	−68.2963	3880
9	Corapi	CORA	−17.5393	−68.3060	3806
10	Huarejani	HUAR	−17.4382	−68.3152	3896
11	Pokullita	POKU	−17.3840	−68.2294	3994
12	Huancarames	HUAN	−17.3601	−68.1123	3901
13	Copani	COPA	−17.3286	−68.0553	3872
14	Patacamaya	PATA	−17.2604	−67.9480	3804
15	Pumasani	PUMA	−17.0774	−67.9735	3955
16	Pinalla	PINA	−16.9432	−68.1110	3980
17	Pocohota	POCO	−16.7519	−68.1923	3980
18	Ventilla	VENT	−16.6223	−68.1747	3960
19	La Paz	LAPZ	−16.5363	−68.1000	3300
20	Vinto Pampa	VIPA	−16.4679	−68.0798	3500
21	Incachaca	INCA	−16.4085	−68.0480	4366
22	Rinconada	RINC	−16.3237	−68.0196	4210
23	Unduavi	UNDU	−16.3312	−67.9495	3590
24	Cota Pata	COTA	−16.2849	−67.8496	3219
25	Chuspi Pata	CHUS	−16.3050	−67.8152	3000
26	Yungas	YUNG	−16.2344	−67.7935	2000
27	Puente Mururata	PUEN	−16.1658	−67.7285	1100
28	Hotel du Planteur	HOTE	−16.0421	−67.6643	1100
29	San Pedro de Leon	SPDL	−16.0047	−67.6193	930
30	San Silverio	SILV	−15.9236	−67.5415	970
31	Colonia Saonedra	CBSA	−15.8494	−67.5275	634
32	Colonia Bartos	BART	−15.7428	−67.5028	927
33	Thee	THEE	−15.6462	−67.4262	1003
34	Rio Beni	BENI	−15.5674	−67.3711	489

axial symmetry (Table 1; Fig. 1). Thus, within limits imposed by usable roads, the seismic profile is made up of two nearly parallel segments (stations 1–14 and stations 18–34) trending about N45°E, connected by a N330°E segment where the road sweeps round the foot of the Eastern Cordillera. Although the network is suitable for 2-D tomographic studies, its quasi-linear shape is not ideal for locating earthquake hypocentres. To improve the geometry of the array for hypocentral determinations, we used only events which were also recorded by Bolivian permanent stations (Table 2; Fig. 1). Five of these stations, built by the French LDG (Laboratoire de Détection Géophysique) (BOA to BOE), are equipped with vertical short-period seismometers ($T_0 = 1$ s); the seismic signal is transmitted by radio to the San Calixto Observatory in La Paz. The LPB station belongs to the WWSS Network.

The arrival times at the permanent stations were taken from the local earthquake bulletin of LDG and those of the temporary network were read by the authors. The reading technique, direct from a computer screen, gives a precision on P-arrival times of about 0.05 s. Since only vertical seismometers were used, special attention was paid to S-waves readings, and we carefully picked only the very clear phases. Considering S-waves frequency content, we estimate the precision on S-arrival times to be better than 0.5 s. An example of local earthquake recorded by the network illustrating the quality of the data is shown in Fig. 2.

The local earthquakes were located using spherical earth equations with travel-time tables of Herrin (1968) for P-waves and travel-time tables of Randall (1971) for S-waves. These tables can be considered to approximate, to a first order, the velocity structure

of the region under study. Travel times were corrected for station elevation, assuming the same velocity as in the first layer of the Herrin model. As a first step, we computed the location of events reporting more than fifteen arrival times with a minimum of 2 S-waves. We performed a number of trials with various initial depths. Next, we kept only those events that met the following criteria: convergence of the hypocentral depth to the same value irrespective of the initial depth; distance to the nearest station less than twice the hypocentral depth; and at least two S-wave arrival times.

Seventy events passed through these tests; 65 are related to the subduction zone (depths greater than 90 km) and five are crustal events (depths less than 10 km). The proportion of crustal events is small because of the condition concerning the minimum distance. On average, 24 phases were used for a hypocentral location. For the deep events, the mean standard error is 10 km with a standard deviation of ± 3.5 km for the epicentral location, and 10 ± 5 km for the depth. The distance to the nearest station is in the range 20– – 180 km, with a mean value close to 100 km; thus, for almost all the events, the minimal distance is of the same order of magnitude as the depth. The azimuthal gap (i.e., the maximum azimuthal aperture viewed from the epicenter where no stations are located) is high, 290° on average, however, this is acceptable bearing in mind the distance to the closest station and hypocentral depth. The complete data set includes about 1600 arrival times of which 1200 are P-wave arrival times.

The location of the 65 deep events is presented in map view in Fig. 3. The seismic activity lies at the western side of the network and during the four months that the network was operated, most of the local earthquakes we located occurred in the depth range 100–160 km. The deeper part of the subduction zone showed modest activity with five events occurring deeper than 200 km.

The validity of the hypocentral location process was checked using a complementary test. For a set of synthetic hypocentres, we computed the P- and S-wave arrival times at the 40 stations used in this study. We then randomly selected a number of arrival times and relocated the synthetic events using the same tables as for the local events. The synthetic events were choosen on the 69.5°W meridian, at

Table 2
Permanent stations coordinates

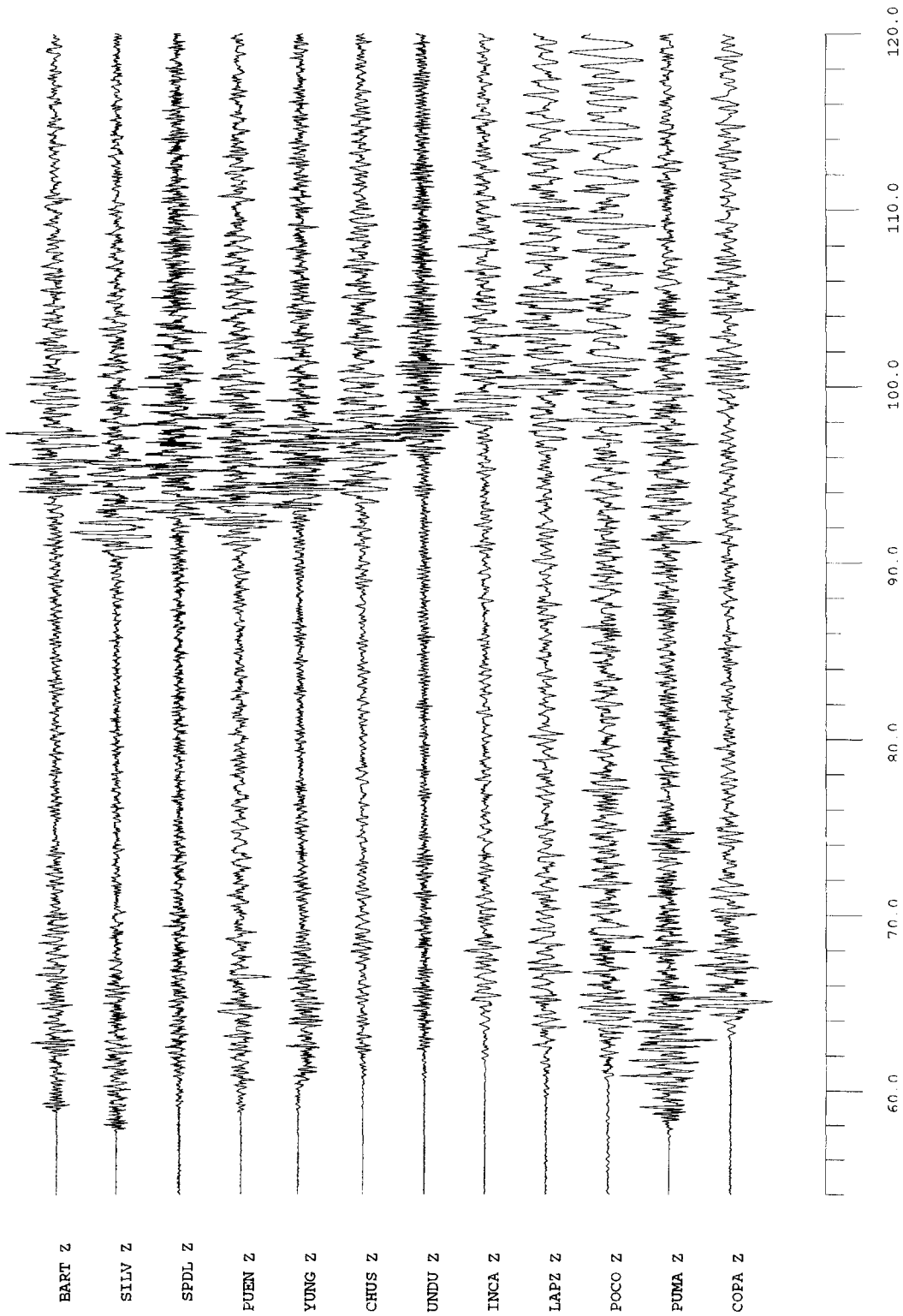| Name	Code	Latitude (°S)	Longitude (°W)	Altitude (m)
Zongo	BOA	−16.2691	−68.1241	4397
Banderani	BOB	−16.1375	−68.1319	3960
Huaylipaya	BOC	−16.0508	−68.0042	1670
	BOD	−16.6374	−68.5981	4230
	BOE	−16.8127	−67.9821	4325
La Paz	LPB	−16.5327	−68.0925	3272

Fig. 2. Example of local event used in this study: November 11, 1990, 20:00. The time scale is indicated below. Traces are plotted with respect to the absolute time. Stations codes are given in Table 1.
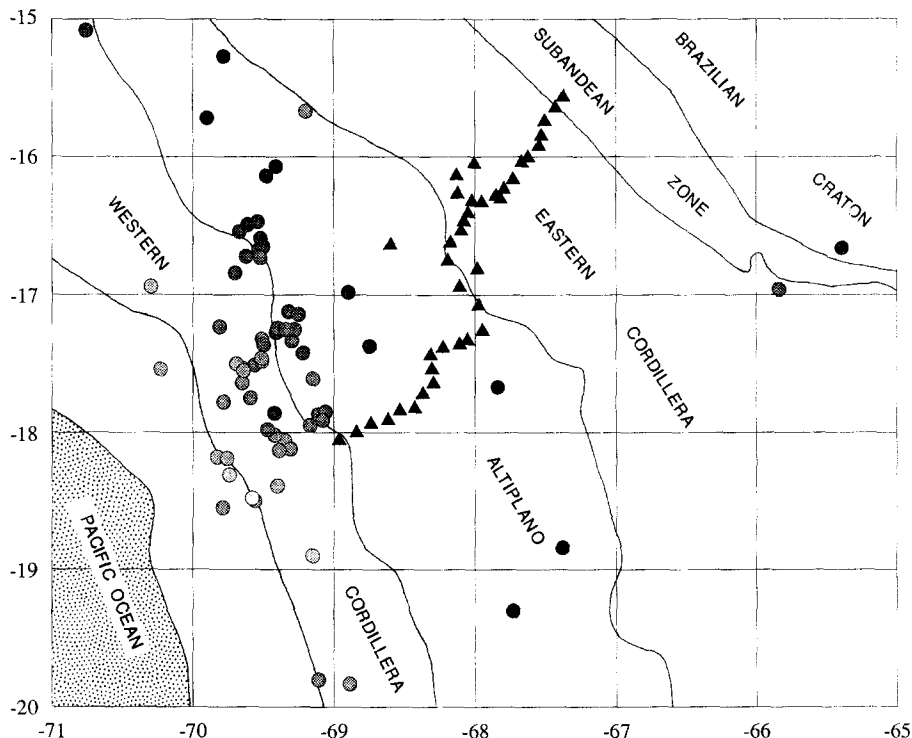
Fig. 3. Distribution of stations and events used for the Local Earthquake Tomography together with the morphostructural zoning of the Central Andes. The shaded circles show the initial epicentral locations of the local events, the darker the deeper. The solid triangles show the position of permanent and temporary seismic stations.

latitudes varying from 16 to 19°S and at a mean depth of 120 km. We performed many relocation trials with various initial hypocentral positions, different subsets and numbers of stations, keeping the same selection criteria as before. The mean difference between the initial positions and the relocations is 10 km for the horizontal coordinates and 14 km for the depths. The error does not depend on the number of phases used for the computation. Thus, the uncertainty is the same on the synthetic hypocentre relocation and on the event location, it is about 10% of the mean distance between the events and the array. As we neither perturbed the velocity model from the one used in the hypocentral determination, nor attached random errors to the synthetic arrival time data, we can assume that the standard error on hypocentral locations represents the minimum uncertainty on the position of the events related to the subduction zone.

For each station, we drew histograms of the P-

and S-wave residuals. The P-wave residual histograms are gaussian in form and the S ones are more diffused. After removing the values higher than $+/-4$ s, we computed the mean P-wave residual at every station for the 65 deep events. These residuals are plotted along the profile in Fig. 4, together with the main structural features. West of the San Andres fault, residuals are negative; they increase abruptly crossing this fault zone ($+0.55$ s between stations 5 and 7). Residuals remain positive to the Cordillera Real fault zone (CRFZ), with maximum values at the western flank of the Cordillera. Crossing the CRFZ, a rapid decrease is observed on the plot; the amplitude of the mean residual variations reaches 1 s between stations 20 and 24. Negative residuals are observed beneath the axial zone of the Eastern Cordillera; east of the Main Andean Thrust (MAT), residuals are about zero. Overall, the local earthquake mean P-wave residuals are strongly correlated with the structural units presented in Fig. 1 and they

are consistent with a simple qualitative model consisting of a low-velocity zone beneath the Altiplano Basin and the western flank of the Eastern Cordillera (between stations 7 and 20), flanked by two high-velocity zones, beneath the Western and Eastern Cordilleras.

3. Inversion study

3.1. Inversion method

The tomographic inversion method used is that developed by Thurber (1983) for the iterative simultaneous inversion of P-wave arrival-time data for a 3-D velocity structure and hypocentral parameters. The program used is the latest version of the program adapted by Eberhart-Phillips (1986) which includes the inversion of S-wave data. P- and S-wave arrival times are inverted independently to produce separate P- and S-wave velocity models.

The parametrization of the region under study is achieved by assigning velocity values at fixed points on a non-uniform 3-D grid. The velocity at any point of the model is linearly interpolated between the nodes surrounding it. This process assumes a continuous velocity field and produces a solution with smooth changes in velocity in contrast to using block models.

An approximate ray tracing algorithm (ART,

Thurber, 1983), is used to calculate travel time between station and receiver. Among a set of smooth curves connecting the source and the receiver, it selects as an approximation of the true ray path the one with the shortest time. Then, a pseudo-bending method is used and the ray path is perturbed to satisfy the criterion that the true ray path curvature is perpendicular to the component of the local velocity gradient normal to the path at each point.

The parameter separation method (Pavlis and Booker, 1980) enables the separation of the velocity and hypocentres calculations into equivalent subsets of equations which are computationally manageable.

3.2. Parametrization

The events selected, i.e., 65 deep local events, provide a good quality data set with regard to the stability of hypocentres and precision of arrival times. On the other hand, the spatial distribution of ray paths is not even, the majority of the events being recorded towards the western side of the network; moreover, in the region under study, it was not possible to improve the ray path distribution by including stations and events outside the modelled area towards the east, as suggested by Eberhart-Phillips (1993), because of the lack of seismic stations in the sub-Andean zone. Thus, the possible effects of this uneven spatial distribution have to be carefully considered in the inversion results. The inversion
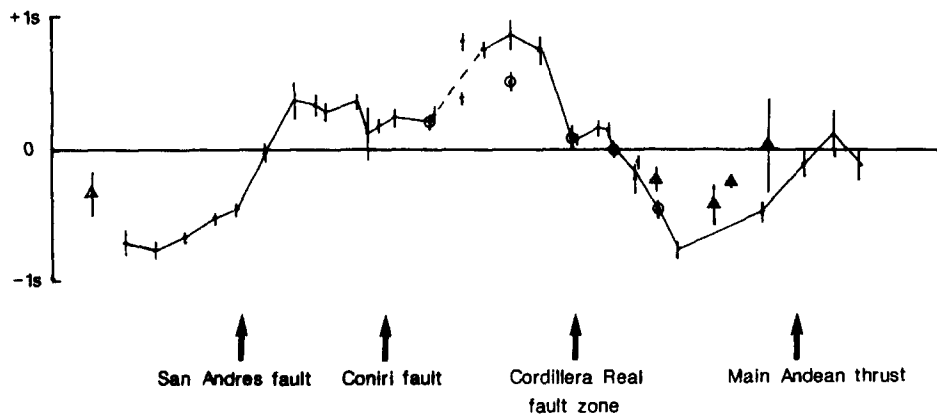

Fig. 4. Mean P-wave residual at every station for the 65 deep events. They are plotted along the seismic profile, with the corresponding standard errors, together with the main structural features. The dots represent temporary stations which registered more than ten events, the triangles represent temporary stations which registered less than ten events, the circles represent the permanent Bolivian stations.

model obtained by teleseismic tomography from a completely independant data set provides the basis for discussion later in this paper.

For the initial P-wave velocities, we chose, as for the teleseismic inversion, a smoothed version of previous velocity models obtained by various methods in the central Andes (Dorbath et al., 1993). The S-wave velocities were initially set by using a V_p/V_s ratio of 1.75, which is the mean value obtained from a global Wadati plot. The velocity grid was aligned north–south. The horizontal grid spacing was one third of a degree in the central part of the modelled area, underneath the seismic stations, and larger outside this zone. The starting model (Table 3) was made of seven layers of grid points from the surface down to the maximum depth of hypocentres.

The LET method we used combines parameter separation and a damped least-squares inversion. A reasonable choice for the damping value was obtained following a practical scheme comparable to the one developed by Eberhart-Phillips (1986). We constructed "trade-off" curves comparing the resolution and the error on the solution in order to get the optimal value which substantially increases the resolution without introducing large velocity variations.

3.3. Stability of the solution

The stability of the solution has been tested by different methods. We tested several nodal configurations: changing the horizontal spacing and the depth distribution of grid points, or rotating the velocity grid by 45°. These hardly modify the solution. A slight variation observed in the velocity values is probably due to the change in the number of obser-

Table 3
Initial P- and S-wave velocity model

Layer	Depth (km)	V_p (km/s)	V_s (km/s)
1	0	5.0	2.85
2	20	6.0	3.43
3	40	6.5	3.71
4	60	6.8	3.88
5	80	8.0	4.57
6	160	8.2	4.70
7	220	8.4	4.79

vations at each grid point. In the same way, variations of initial velocities, or variations of the velocity model layer thicknesses, produce a weak change in the final focal depths of the events and have a negligible effect on the final velocity model. Therefore, the final velocity model is relatively independent of the initial nodal configurations and remains stable.

3.4. Resolution

The reliability of the inversion is mainly indicated by the resolution matrix. The diagonal resolution element indicates how influenced the velocity solution is by the space immediately surrounding the grid point. Then, if the diagonal element is the largest, the velocity solution is well resolved at that grid point. On the other hand, the off-diagonal elements of the resolution matrix at a given grid point demonstrate the influence of other grid points on the velocity solution at that point.

For the five shallower layers of grid points, the diagonal resolution elements range from 0.01 to 0.72, with an average of 0.26 for the P-wave velocity model, and from 0.01 to 0.56, with an average of 0.20 for the S-wave velocity model. Below 80 km, the values become very low; due to the uneven distribution of earthquakes and stations, deep nodes are not well sampled by rays. Drawing the velocity models, we take into account only the nodes where the diagonal element of the resolution matrix is greater than 0.10.

The coupling between neighbouring nodes has been checked by analysing the complete resolution matrix. For the results presented later along the two lines drawn in Fig. 1, we show the values of the complete resolution matrix for the P-wave velocity model for the relevant nodes (Fig. 5). It is worth noting that, except for two nodes in the first layer, the diagonal resolution element is everywhere the largest. The influence of horizontally adjacent nodes is weak. The vertical coupling is significant in the crust (three first layers) but negligible underneath. The reliability of the S-wave velocity model has been checked in the same way. The complete resolution matrix presents the same feature as for the P-wave model at every grid point: the amplitude of the values are weaker, but the relative amplitudes

a)
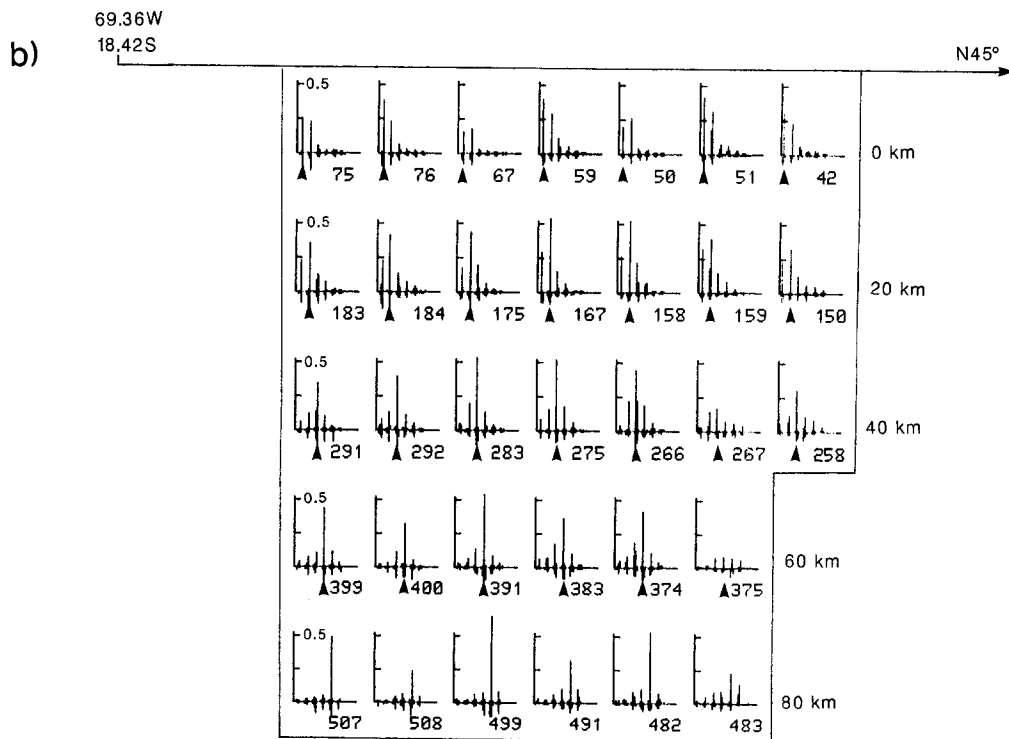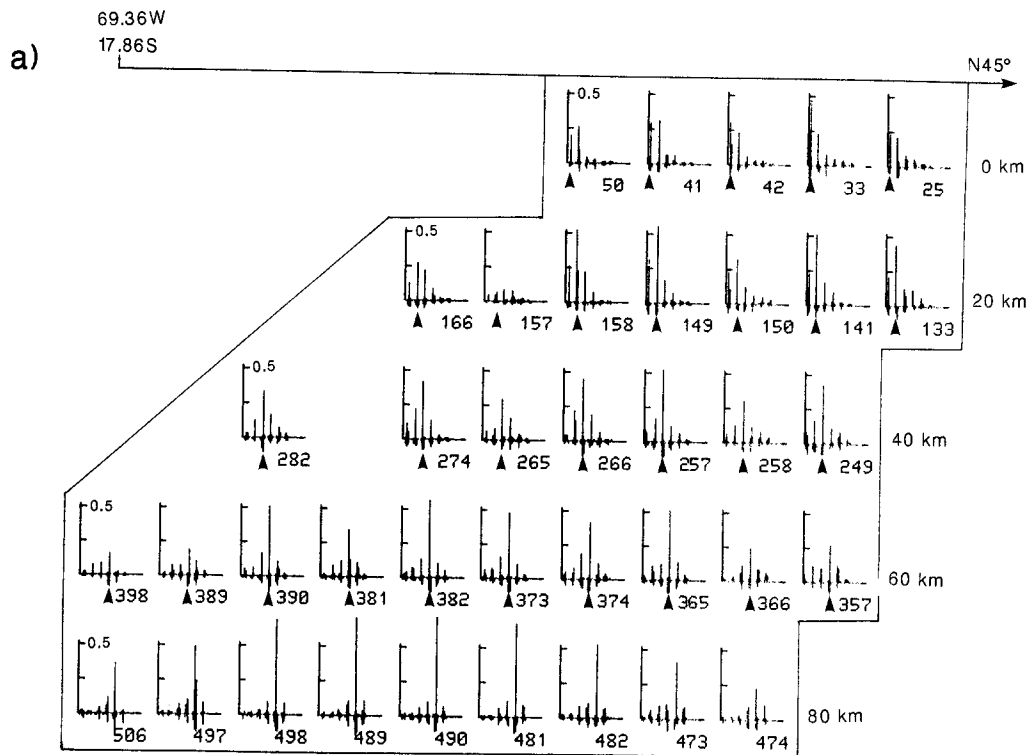
between the diagonal and the off-diagonals elements are the same.

For the final model, the average standard error is 0.09 km/s for P-wave and 0.08 km/s for S-wave, it is about 2% of the lowest velocity of the model, while the average velocity variations are of the order of 5–10%. Therefore the velocity variations are significant with respect to the uncertainties.

The initial data variance was 0.504 s^2 for P-waves (0.577 s^2 for S-waves), after four iterations it becomes 0.068 s^2 (0.291 s^2), thus the travel-time variance reduction is 87% (50%).

4. Results

4.1. Earthquake locations

Using the P- and S-wave velocity models obtained by the LET inversion, we relocated the 65 events that occurred beneath our area of study. A comparison of the original and final event locations indicates a random variation of a few tenths of a degree. The variations of epicentral positions are smaller than 0.2° for 75% of the events, and smaller than 0.1° for 31%; the mean depth variation is 4 km. The amplitude of these variations is similar to the standard errors given for the original location of events using travel-time tables.

This relocation allows us to define precisely a part of the subducted slab of the Nazca plate underneath northen Bolivia. The most recent studies concerning the shape of the subducted Nazca plate (Hasegawa and Sacks, 1981; Grange et al., 1984; Cahill and Isacks, 1992) show that isodepth lines trend in a N320°E direction below northern Bolivia. We then present the final hypocentral locations on a vertical cross section following the northern line of Fig. 1 (Fig. 6). This line is well situated with respect to the hypocentres locations as well as to the resolved part of the velocity model, and its trend follows the maximum gradient of the subduction.

The image of the subduction zone provided by this method is comparable to the results of the previous studies. The part of the slab defined by this study deepens from 90–100 km under the western part of the Western Cordillera to 180–200 km under the eastern part of the Altiplano. As expected, the Nazca plate is being subducted beneath Bolivia with a uniform dip angle of about 30°.

It seemed interesting to investigate the stress regime in the subducted plate. Due to the geometry of the network, it was not possible to directly construct well-constrained individual focal mechanisms from the first P-wave motions which had been read for these local events. However, assuming that an unique stress tensor can explain the whole data set, we used the method developed by Rivera and Cisternas (1990). This algorithm allows the simultaneous estimation of the orientation and shape of the stress tensor for the subducted slab and the individual fault plane solutions for the population of earthquakes. The input data are the polarities of the P-wave arrival and take-off angles for the set of source–station pairs. We only kept the events with more than eight polarities and for which one of the focal plans was constrained. We performed the calculation using 47 events with fifteen polarities on average. A normalized likelihood function of 97% was obtained, and 98% of the polarities were explained by the extensional stress tensor calculated. The focal mechanisms presented in Fig. 6 are individual mechanisms deduced from this inversion of polarities. They essentially show downdip extension as it is usual for intermediate-depth earthquakes in this area. Grange et al. (1984) for southern Peru or Comte et al. (1992) for northern Chile, on either side of the studied area, obtained very similar results, but they found a direction of extension parallel to the direction of the convergence as it is expected. In our case, the direction of the extension shows a difference of about 30° with the convergence. This discrepancy may be a consequence of the poor resolution of the focal solutions due to the linear shape of the network.

Fig. 5. Values of the complete resolution matrix for the P-wave velocity model for the nodes used in the northern cross section (a) and in the southern cross section (b). The numbers of the nodes are written in bold characters below each diagram. For each node, the value of the diagonal element of the matrix is pointed out by an arrow. Except for two nodes in the first layer, the value of the diagonal resolution element is everywhere the largest. Lateral and vertical coupling are weak below the crust.
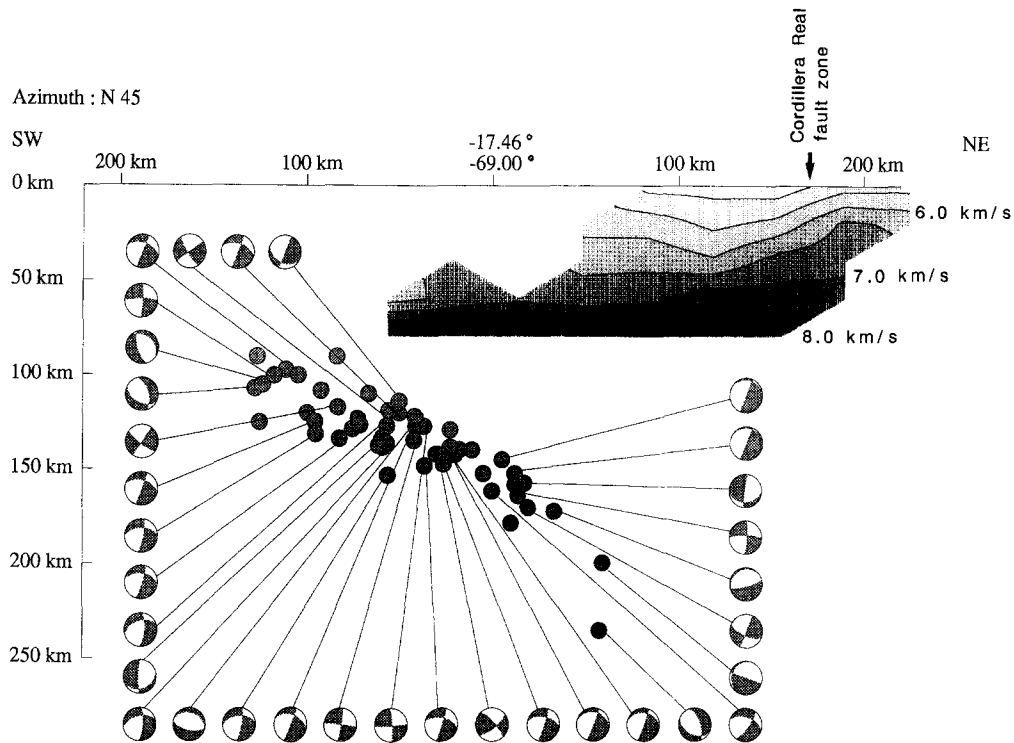
Fig. 6. Vertical cross section along the northern dashed line (Fig. 1) through the relocated hypocentres and the P-wave velocity model (no vertical exaggeration). The location of the downgoing slab is well defined by the seismicity. The best resolved focal mechanisms are presented (lower hemisphere, equal-area projection). The Altiplano Basin, southeast of the Cordillera Real fault zone, is underlain by low velocities (5.5 km/s down to 20 km). The Moho is defined by the 7.5 km/s iso-velocity line, and has a mean depth of 66 km.

4.2. P-wave velocity model

The P-wave and S-wave velocity models generally show a similar pattern of velocity variations. However, due to fewer observations of S-wave arrival times (only a quarter of the complete data set are S-wave arrival times), the resolution of the S-wave velocity model is reduced and many zones of the studied area have too low a resolution to be taken into consideration. Therefore, we will only discuss in detail the P-wave velocity model; on the other hand, the V_p/V_s ratio will be considered in the areas where both velocity models are resolved.

A cross section through the P-wave velocity model along the northern line, together with the cross section through the hypocentres, is shown in Fig. 6. In the crust, iso-velocity lines emphasize the Altiplano Domain. A slow zone is observed west of the CRFZ with velocities less than 5.0 km/s down to 7 km and less than 5.5 km/s down to about 20 km. Moreover,

iso-lines 5.5–6.5 km/s are more than 25 km deeper under the Altiplano than under the Eastern Cordillera. The low-velocity zone, whose maximum thickness is observed under the Altiplano Basin, is clearly associated with the sedimentary infill of this basin. Where the Cenozoic detrital series along the zone of the profile is more than 10 km thick, the total thickness of sedimentary rocks, including the underlaying Paleozoic, Mesozoic and Paleogene beds, is about 20 km (Meyer and Murillo, 1961; Ascarrunz, 1973a,b). Therefore, the low-velocity zone may be explained by the thickness of the sedimentary infill, and it is not necessary to introduce the hypothesis of a volcanic or plutonic origin.

Even if the vertical coupling between adjacent grid points is weak, the information is spread along the ray path connecting hypocentre and station. Thus, the transition between the crust and the upper mantle is marked by a narrowing of the iso-lines. Taking the iso-line 7.5 km/s as an estimation of the bottom of

the crust, we find a mean Moho depth of 66 km. This is in good agreement with the results of the previous geophysical studies (see Dorbath et al., 1993, for a review), which agree with a crustal thickness beneath the Altiplano of the order of 60–70 km.

A detailed picture of the superficial P-wave velocity is presented in Fig. 7 together with the main structural features. The consistency between velocity zones and structural units is good. The lowest veloci-

ties (below 4.75 km/s) are observed between the San Andres and Laurani faults, associated with the Cenozoic series of the Altiplano Basin. The western flank of the Eastern Cordillera, east of the Laurani fault up to the CRFZ, where Paleozoic series are 10–12 km thick (Sempere et al., 1990), is characterized by intermediate velocities (up to 5.0 km/s). A fast zone (up to 5.5 km/s) corresponds to the axial zone of the Eastern Cordillera, where the main part of the outcrops are formed by the Ordovician series.
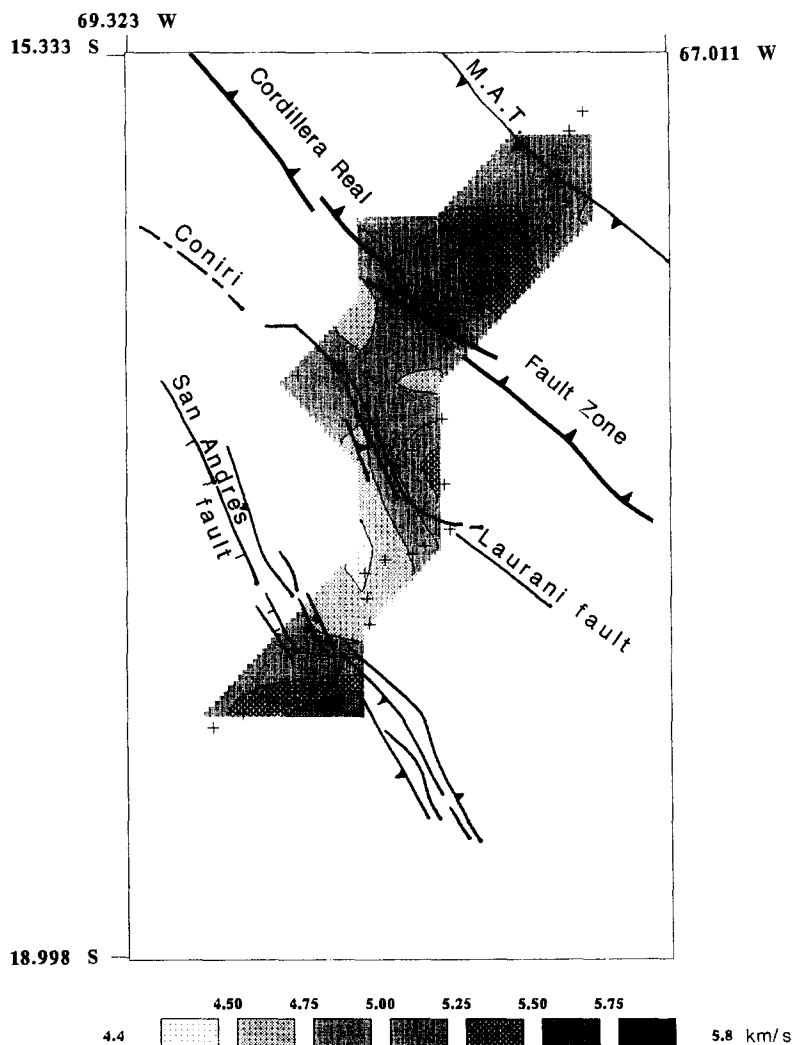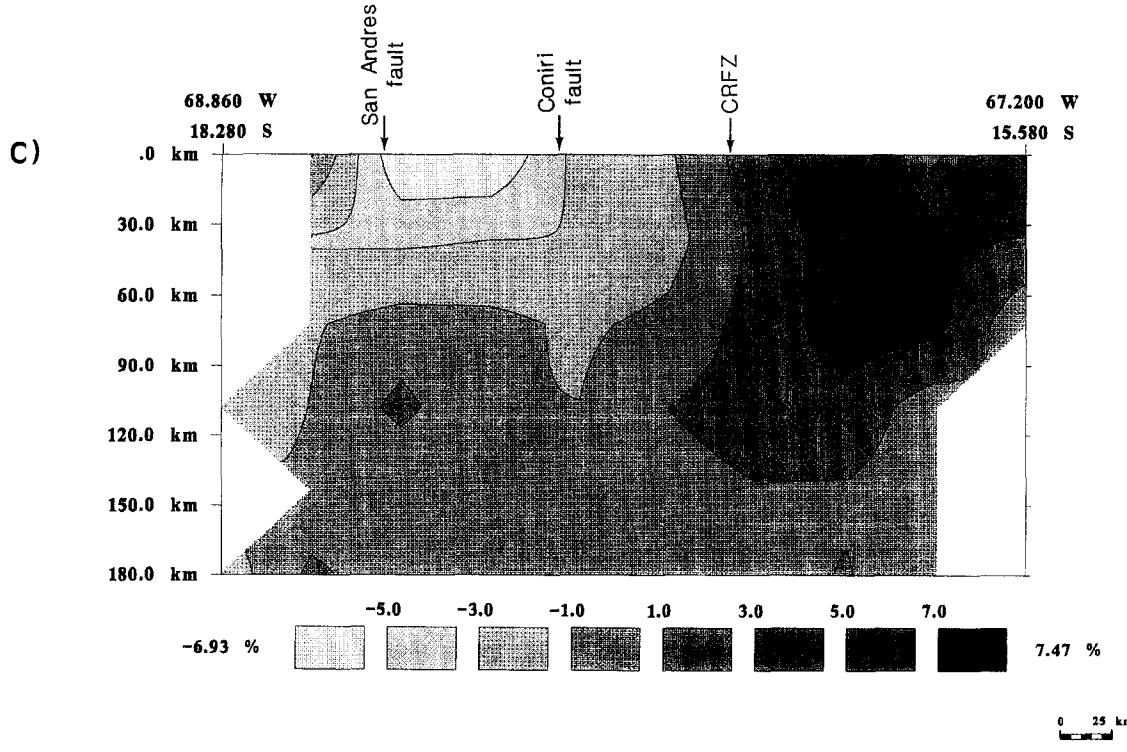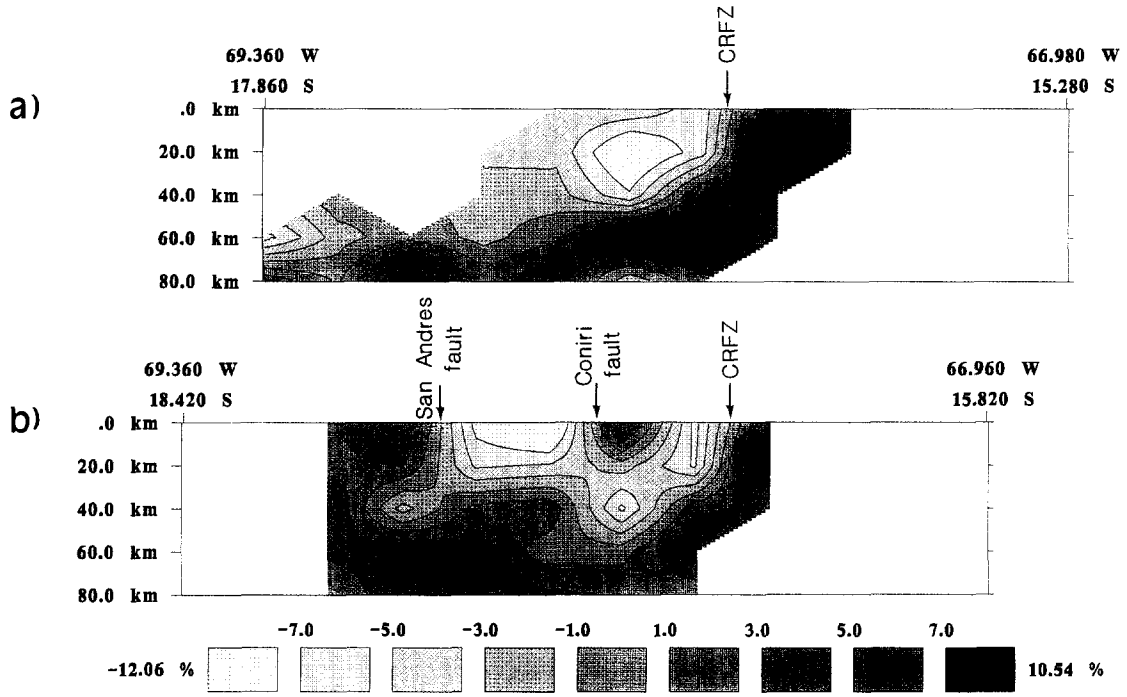

Fig. 7. Smoothed P-wave velocity in the first layer of the 3-D model, together with the main structural features. To get the smooth pattern, we applied a bilinear interpolation function to the discrete perturbations within each horizontal layer. This smoothing algorithm preserves the amplitudes for individual nodes of the original discretization. The horizontal grid spacing is 0.33°. Higher velocities correspond to darker shading.

a)

69.360 W
17.860 S

66.980 W
15.280 S

CRFZ

.0 km
20.0 km
40.0 km
60.0 km
80.0 km

b)

69.360 W
18.420 S

66.960 W
15.820 S

San Andres fault

Coniri fault

CRFZ

.0 km
20.0 km
40.0 km
60.0 km
80.0 km

-12.06 %   -7.0   -5.0   -3.0   -1.0   1.0   3.0   5.0   7.0   10.54 %

c)

68.860 W
18.280 S

67.200 W
15.580 S

San Andres fault

Coniri fault

CRFZ

.0 km
30.0 km
60.0 km
90.0 km
120.0 km
150.0 km
180.0 km

-6.93 %   -5.0   -3.0   -1.0   1.0   3.0   5.0   7.0   7.47 %

0   25 km

DVp CROSS SECTIONS

High velocities are also seen southwest of the San Andres fault, in the western Altiplano. They can be associated with the Precambrian basement observed in drill data at 2745 m depth (San Andres borehole, Lehmann, 1978).

4.3. Velocity perturbations

In order to make the LET results more easily comparable with those obtained by the teleseismic tomography, we present our final model in terms of velocity perturbation. The narrowness of the area horizontally sampled together with the axial symmetry of the Andean chain let us draw the models along two vertical cross sections (see Fig. 1). These two lines, trending N45°E, are perpendicular to the tectonic structures and cross the best resolved parts of the velocity models. The northern line is suitable to study the changes across the CRFZ, whilst the southern is suitable for studying the structure of the Altiplano. The smoothed images down to 80 km for these cross sections through the P-wave velocity perturbation model are shown in Fig. 8a and b, while Fig. 8c presents the vertical cross section through the teleseismic inversion model from Dorbath et al. (1993). The amplitude of the velocity perturbations in the LET model, more than 20%, is nearly twice the perturbations for the teleseismic tomography. At first sight, both LET and teleseismic velocity perturbations models show two primary features: a horizontal gradient at the CRZFZ and a vertical gradient below the Altiplano basin. They are very similar considering the vertical smearing and broadening of features in the teleseismic inversion. On the other hand, the LET model offers much higher spatial resolution and is closely related to the structural units.

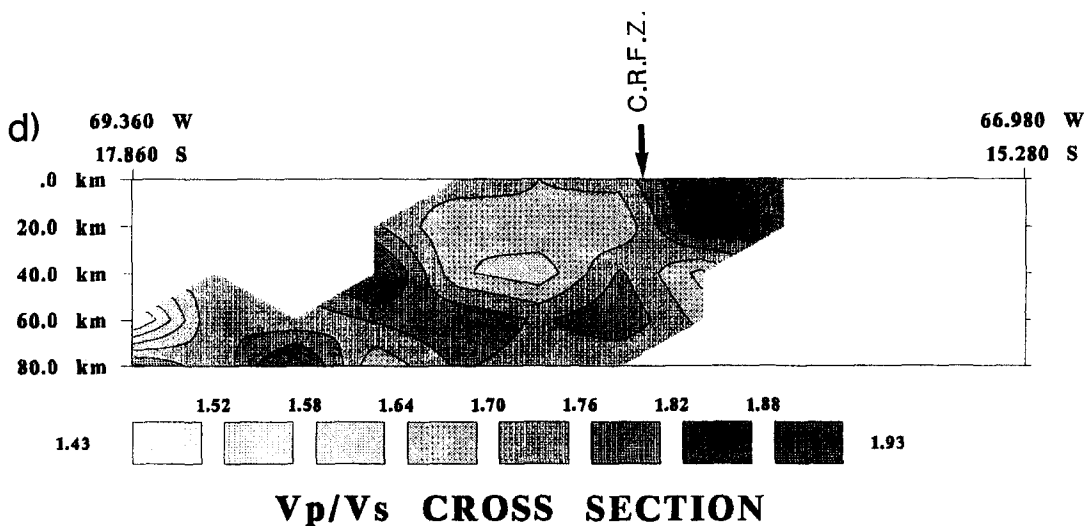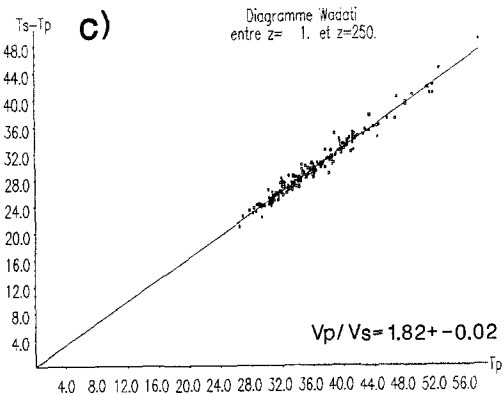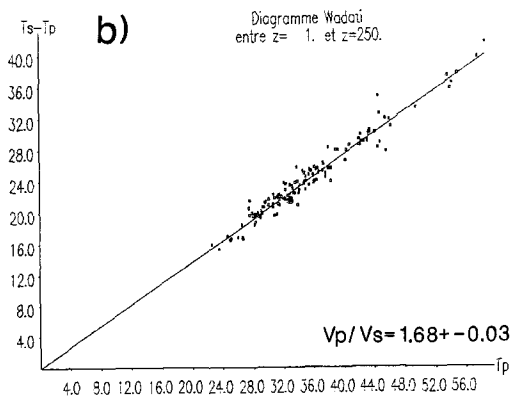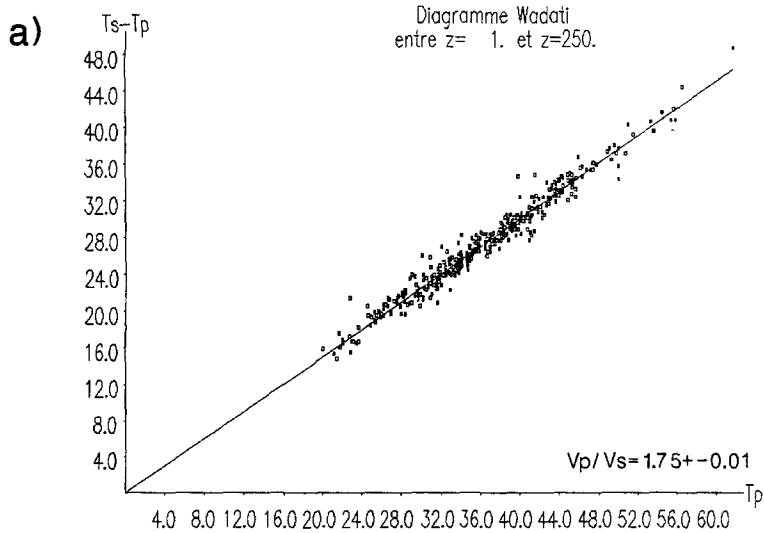On the southern cross section (Fig. 8b), the presence of the Altiplano Basin is clearly indicated by a well-marked slow zone which extends down to at least 40 km. The limits of this low-velocity zone are sharply defined and closely coincide with the bordering San Andres and Coniri faults. The amplitude of the velocity perturbations and their depth extension (more than 5% down to 20 km), again emphasizes the thickness of the sedimentary infill. In the vicinity of station 14, where the Coniri fault is transformed to the Laurani fault through a zone of hidden transfer faults (Ayo Ayo fault zone, Ascarrunz, 1973a,b), a small area of higher velocity is observed in the upper crust east of the Coniri fault. This velocity anomaly may be due to the complexity of this zone.

The velocity contrast between the western flank and the axial zone of the Eastern Cordillera is strongly marked in the P-wave velocity model (Fig. 8a). The velocity perturbation gradient observed between the slow zone, associated with the Altiplano Basin and the western flank of the Cordillera, and the fast zone, associated with the Eastern Cordillera, is very strong (from -5 to $+5\%$ in 25 km). As in the teleseismic model, the CRFZ appears as a major frontier. The highest velocity perturbation zone (more than $+7\%$) is concentrated beneath the axial zone of the Eastern Cordillera, but the fast zone extends in depth beneath the western flank of the Cordillera and the Altiplano to the southwest. Thus, in the LET model, the velocity contrast associated at the surface with the CRFZ is subvertical from the surface down to 30–40 km and then dips towards the southwest with a lower angle down to 70 km.

4.4. V_p / V_s ratio

Before studying the V_p / V_s models calculated during the simultaneous inversion, we examined the composite Wadati diagrams plotted with P- and S-wave travel times (Fig. 9a–c). We pointed out earlier that, for the complete region, the V_p / V_s ratio is 1.75,

Fig. 8. (a) Vertical cross section down to 80 km through the P-wave velocity perturbation model, along the northern dashed line of Fig. 1. No vertical exaggeration. The velocity perturbations are expressed in percent. Velocities higher than the reference correspond to positive values, velocities lower than the reference correspond to negative values. (b) Similar vertical cross section along the southern dashed line of Fig. 1. Note the close coincidence between the velocity perturbation changes and the main structural features. (c) Vertical cross section down to 180 km through the velocity perturbations of the 3-D teleseismic inversion model, along the dotted line of Fig. 1. No vertical exaggeration. More detail can be found in Dorbath et al. (1993). The amplitude of the velocity perturbations is more than 20% in the LET model, it is nearly twice the amplitude of the perturbations for the teleseismic tomography. Both models show the same primary features: a horizontal gradient at the CRZFZ and a vertical gradient below the Altiplano.

a)

Diagramme Wadati
entre z= 1. et z=250.

Ts-Tp

Vp/Vs= 1.75+−0.01

Tp

b)

Diagramme Wadati
entre z= 1. et z=250.

Ts-Tp

Vp/Vs= 1.68+−0.03

Tp

c)

Diagramme Wadati
entre z= 1. et z=250.

Ts-Tp

Vp/Vs= 1.82+−0.02

Tp

d)

C.R.F.Z.

69.360 W   66.980 W
17.860 S   15.280 S

1.52   1.58   1.64   1.70   1.76   1.82   1.88

1.43   1.93

Vp/Vs CROSS SECTION

close to the standard value. We then separated the stations into two groups. The first group, called the Altiplano group, includes all the stations from station 1 to station 19 plus BOD and BOE, that is all the stations west of the CRFZ. The second group, called Cordillera group, includes all the remaining stations which are situated east of this fracture zone. The Wadati plots for these two groups are very different. The V_p/V_s ratio is low for the Altiplano, 1.68, and very high for the Cordillera, 1.82.

A cross section through the V_p/V_s ratios along the northern line displays with more detail consistent features (Fig. 9d). The reduced resolution of the S-wave velocity model makes unreasonable a detailed analysis of the V_p/V_s ratios, thus only the large anomalies will be considered.

Under the Altiplano Basin, down to 60 km, the velocities are also low for P- as well as for S-waves. The low value of the ratio is due to the fact that P-wave velocities are in proportion much lower than S-wave velocities and the anomaly is concentrated in the crust. On the other hand, the very high value of the ratio observed for the Cordillera is localized in the upper crust and corresponds to different behaviour of P- and S-wave velocities in this region: V_p values are high when V_s values normal to low. Another large zone with hight V_p/V_s ratio is observed southwest of the Altiplano below 40 km; this area is not sampled at shallower depths. In this zone, P-wave velocities are normal to slightly slow when S-wave velocities are slow. Thus this representation shows more precisely the zoning of different V_p/V_s ratios, i.e., of different Poissons ratios.

5. Discussion

The LET study allowed us to give a new estimate of the Moho depth below the Altiplano of northern Bolivia: 66 km, taking the 7.5 km/s iso-velocity line as an estimation of the bottom of the crust. This value is within the range of the Moho depths found under the Altiplano by different geophysical methods

[seismic profiles (Ocola et al., 1971; Wigger, 1988), surface waves (Cisternas, 1961; James, 1971) and gravimetry (Strunk, 1990; Fukao et al., 1989)]. In a 3-D study of the velocity structures between the coast and the Western Cordillera in southern Peru, Cunningham et al. (1986) also chose the 7.5 km/s velocity contour as an indicator of the Moho depth. Their results suggest a crustal thickness of about 70 km beneath the Western Cordillera, the same value as we observe in the southwestern part of our P-wave velocity cross section. The thinning of the crust below the Eastern Cordillera, documented by previous geophysical studies (James, 1971; Fukao et al., 1989) as well as by the teleseismic inversion, is not seen on this velocity contour. However, due to the hypocentral distribution, the northeastern end of the model is not sampled at that depth. However, one can note that the iso-7.0 km/s line is higher by more than 12 km between the Altiplano and the axial zone of the Cordillera. It therefore seems reasonable to assume that higher velocities follow the same trend, and thus give evidence of the thinning of the crust towards the northeast. A decrease of the Moho depth from about 65 km under the Altiplano to about 55 km under the Eastern Cordillera would confirm that the Eastern Cordillera is not locally compensated, as was previously deduced from gravity studies (Kono et al., 1989) and teleseismic inversion. In this eastern edge of the central Andes, the thermal effects are small and compression is dominant; the crust pushed by the westward movement of the South American plate is shortened by reverse faulting in the Eastern Cordillera and the sub-Andean zone.

When compared with the teleseismic inversion, LET brings us a much more detailed picture of the crustal structures: particularly the limits bordering the structural units are sharply defined and their coincidence with surface geology is excellent. In Fig. 8b is shown that the morphostructural zoning observed at the surface continues at depth. The partition of the Altiplano Domain into two distinct units is sharp; the velocity contrast between the last western Altiplano and the very slow Altiplano Basin is

Fig. 9. (a) Plots of P-wave travel time versus S–P-wave travel time (Wadati plot) for arrivals from all deep events at all the seismic stations. (b) Wadati plot for the Altiplano stations (stations 1–19, LPZ, BOA and BOE). (c) Wadati plot for the Cordillera stations (stations 20–34, BOB, BOC, BOD). (d) Vertical cross section through the V_p/V_s ratio obtained during the LET inversion, along the northern profile of Fig. 1.

located under the San Andres fault zone and is well marked down to 20 km. The continuation at depth of the velocity gradient supports the interpretation of Martinez (1980); the San Andres fault zone is interpreted to be the eastern border of the Precambrian Arrequipa terrane, which is the remainder of the late Precambrian–Early Cambrian Brasilides (Lehmann, 1978), consisting of reworked rocks dated at 2000–1100 Ma (Cobbing et al., 1977). The Laurani–Coniri fault is less marked on the velocity model. Although this fault is the limit between the Altiplano Basin and the western flank of the Eastern Cordillera, it is located in the morphological Altiplano and does not appear as a clear velocity boundary.

Even when such a spatial resolution cannot be obtained by teleseismic tomography, the same major features can be seen on the velocity models obtained by the two independent methods. It is clear on the three cross sections (Fig. 8a–c) that the velocity structure anomaly associated with the Altiplano is concentrated in the crust. The absence of either a P- or S-wave low-velocity anomaly beneath the crust does not support the hypothesis of magma accretion at the base of the crust (Dewey and Bird, 1970) or of lithospheric thinning (Froidevaux and Isacks, 1984) under the Altiplano. Moreover, a crustal root of 62–67 km is necessary to compensate the average topography of the Altiplano (Dorbath et al., 1993). Thus, the mean Mono depth deduced from the inversion together with the velocity model support the hypothesis that the Altiplano is in isostatic equilibrium and mainly crustally compensated.

The steep velocity gradient which corresponds at the surface with the CRFZ is obvious on both models. The velocity contrast, subvertical in the upper crust, appears more or less steeply dipping towards the southwest according to the velocity model. This effect may be partly inherent in the data sets used for the inversions: teleseismic ray paths are subvertical when local events rays mainly come from the southwest of the network, and, even if the vertical coupling is low in both models, the differences in the ray paths may influence the apparent slope of the velocity discontinuity. In any case, beneath 70 km almost no velocity perturbation is observed along the profiles; velocities remain just a little higher underneath the Eastern Cordillera. At that depth, the amplitude of velocity perturbations is about 6%. It was about 4% in the teleseismic tomography, thus comparable, taking into account the maximum amplitude of perturbations. So, although the limit between low- and high-velocity perturbations appears more or less vertical, the distribution of velocity perturbations is similar in both models. This sharp velocity contrast is interpreted as a lithologic boundary, and the relation between the high-velocity anomaly east of the CRFZ and the Brazilian craton has already been documented (Dorbath et al., 1993). Although the representation of the underthrusting of this craton under the Altiplano is somewhat different on the teleseismic and local earthquake tomographies, the results of these independent studies are not consistent with a thin-skinned underthrusting as proposed by Roeder (1988) along the same transect.

An interpretation of the variations of the Poissons ratio along the profile in terms of temperature and pressure conditions needs a more precise knowledge of the petrology of the region than we have. However, some correlations may be noticed between the large-scale V_p/V_s anomalies and some general structural features. The low V_p/V_s anomaly beneath the Altiplano corresponds to very low V_p and low V_s, and is observed underneath the basin and the western flank of the Cordillera. This low anomaly is located in the crust where the Paleozoic to Cenozoic series are the thickest.

On the other hand, the high V_p/V_s anomalies seem essentially controlled by the presence of magmas. The high Poissons ratio value observed in the upper crust of the axial zone of the Eastern Cordillera corresponds to high V_p and low V_s. This anomaly may be caused by the presence of the large granodioritic batholith which makes up the Cordillera Real, the Illimani and the Quimsa Cruz. These Andean plutons which are associated with an important hydrothermalism, may behave differently with respect to P- and S-waves. Southwest of the Altiplano Basin, a marked low anomaly is seen on the V_p/V_s model at depths of 50–75 km; it is mainly due to anomalously low P-wave velocities in the region (Fig. 8a), the S-wave velocities staying close to the starting velocity model due to the low resolution. However, this anomaly is well enough resolved to be considered. It is located beneath the volcanic arc of the Western Cordillera. Cunningham et al. (1986) observed a low mantle S-wave velocity above the part of the slab

subducting with a 30° dip angle. The effect of temperature on the velocity being smaller on S- than on P-waves (Meissner, 1986), then the presence of high temperature involves a low V_p/V_s. Thus this Poissons ratio anomaly may be related to the presence of high temperature associated with the volcanic activity. On the same Andean segment, from Puno (southern Peru) to Peldehue (central Chile), Sacks (1977) observed a low Q anomaly between the subducting lithosphere and the continental lithosphere. Therefore our result is a new evidence of the presence of a mantle wedge beneath the active volcanic arc, above the 30°-dipping subduction.

6. Conclusion

The velocity structure in the crust and the upper mantle beneath the central Andes of northern Bolivia is obtained by the simultaneous inversion of local earthquake arrival-time data for velocity and hypocentral parameters.

The seismicity defines, between 90 and 225 km depth, a part of the slab deeping to the north-northeast with an angle of about 30°. The focal mechanisms of the events generally show normal faulting with a left-lateral strike-slip component.

The P-wave velocity model allows an estimate of the Moho depth underneath the Altiplano. The crust is about 65 km thick beneath the Altiplano; the iso-velocity lines suggest a thinning of the crust by 10 km beneath the Eastern Cordillera.

The local earthquake tomography provides a detailed view of the velocity model. Velocity anomalies, while being consistent with the results of the teleseismic inversion, show a close correlation with the geological and tectonical units. The spatial consistency between the main fault systems and velocity changes is precise. The two fault zones bordering the Altiplano Basin, San Andres and Laurani faults, enclose the well-marked P- and S-wave slow anomaly connected with this basin. The low values of the velocity down to great depths (5.5 km/s for P-waves down to 20 km) emphasize the thickness of the sedimentary infill in this basin. The absence of low velocities beneath the crust does not support the hypothesis of magma accretion at the base of the crust under the Altiplano.

The high P-wave velocity anomaly under the axial zone of the Eastern Cordillera extends down to the bottom of the model. This high-velocity anomaly is bounded to the west by a steeply dipping discontinuity wich corresponds at the surface with the Cordillera Real fault zone. This high-velocity anomaly has been interpreted to be related to the underthrusting of the Brazilian craton (Dorbath et al., 1993). Although the representation of this underthrusting is somewhat different on the teleseismic and local earthquake tomographies, the results of these independent studies do not support the hypothesis of a thin-skinned underthrusting of the Brazilian craton as proposed by Roeder (1988) for the same region.

Finally, the study of the V_p/V_s ratio, in the zones where the S-wave velocity model is well enough resolved, indicates the different behaviour of some parts of the model with regard to P- and S-wave velocities. In particular, the deep low Poissons ratio anomaly observed west of the Altiplano Basin is consistent with the presence of a mantle wedge beneath the active volcanic arc.

Acknowledgements

References

Aki, K. and Lee, W.H.K., 1976. Determination of three-dimensional velocity anomalies under a seismic array using first P

arrival times from local earthquakes, 1. A homogeneous initial model. J. Geophys. Res., 81: 4381–4399.

Ascarrunz, R., 1973a. Estudio estructural de la region norte de la falla Coniri. Ann. 3a Conv. Nac. Geol., Bol. Soc. Geol. Boliv., 19: 75–81.

Ascarrunz, R., 1973b. Contribucion al conocimiento geologico del area comprendida entre los pueblos de Viacha-Corocoro—y Umala. Ann. 3a Conv. Nac. Geol., Bol. Soc. Geol. Boliv., 20: 29–64.

Cahill, T. and Isacks, B.L., 1992. Seismicity and shape of the subducted Nazca plate. J. Geophys. Res., 97: 17,503–17,529.

Cisternas, A., 1961. Crustal structure of the Andes from Rayleigh wave dispersion. Bull. Seismol. Soc. Am., 51: 381–388.

Cobbing, E.J., Ozard, J.M. and Snelling, N.J., 1977. Reconnaissance geochronology of the cristalline basement rocks of the coastal Cordillera of Southern Peru. Geol. Soc. Am. Bull., 88: 241–246.

Comte, D., Pardo, M., Dorbath, L., Dorbath, C., Haessler, H., Rivera, L., Cisternas, A. and Ponce, L., 1992. Crustal seismicity and subduction morphology around Antofagasta, Chile: Preliminary results from a microearthquake survey. Tectonophysics, 205: 13–22.

Cunningham, P.S., Roecker, S.W. and Hatzfeld, D., 1986. Three-dimensional P and S velocity structures of southern Peru and their tectonic implications. J. Geophys. Res., 91: 9517–9532.

Dalmayrac, B., Laubacher, G. and Marocco, R., 1980. Caractères généraux de l'évolution géologique des Andes péruviennes. Trav. Doc. ORSTOM, 122, 501 pp.

Dewey, J.F. and Bird, J.M., 1970. Mountain belts and the new global tectonics. J. Geophys. Res., 75: 2625–2647.

Dorbath, C., Granet, M., Poupinet, G. and Martinez, C., 1993. A teleseismic study of the Altiplano and the Eastern Cordillera in northern Bolivia: new constraints on a lithospheric model. J. Geophys. Res., 98: 9825–9844.

Eberhart-Phillips, D., 1986. Three-dimensional velocity structure in Northern California Coast Ranges from inversion of local earthquake arrival times. Bull. Seismol. Soc. Am., 76: 1025–1052.

Eberhart-Phillips, D., 1989. Active faulting and deformation of the Coalinga anticline as interpreted from 3D velocity structure and seismicity. J. Geophys. Res., 94: 15,565–15,586.

Eberhart-Phillips, D., 1990. Three-dimensional P- and S-velocity structure in the Coalinga region, California. J. Geophys. Res., 95: 15,343–15,363.

Eberhart-Phillips, D., 1993. Local Earthquake Tomography: Earthquake Source Regions. In: H.M. Iyer and K. Hirahara (Editors), Seismic Tomography, Theory and Practice. Chapman and Hall, London, pp. 613–643.

Froidevaux, C. and Isacks, B.L., 1984. The mechanical state of the lithosphere in the Altiplano–Puna segment of the Andes. Earth Planet. Sci. Lett., 71: 305–314.

Fukao, Y., Yamamoto, A. and Kono, M., 1989. Gravity anomaly across the Peruvian Andes. J. Geophys. Res., 94: 3867–3890.

Grange, F., Cunningham, P., Gagnepain, J., Hatzfeld, D., Molnar, P., Ocola, L., Rodrigues, A., Roecker, S.W., Stock, J.M. and Suarez, G., 1984. The configuration of the seismic zone and the downgoing slab in southern Peru. Geophys. Res. Lett., 11: 38–41.

Hasegawa, A. and Sacks, I.S., 1981. Subduction of the Nazca plate beneath Peru as determined from seismic observations. J. Geophys. Res., 86: 4971–4980.

Herrin, E., 1968. 1968 seismological tables for P phases. Bull. Seismol. Soc. Am., 58: 1193–1241.

James, D.E., 1971. Andean crustal and upper crustal mantle structure. J. Geophys. Res., 76: 3246–3271.

Kono, M., Fukao, Y. and Yamamoto, A., 1989. Mountain building in the Central Andes. J. Geophys. Res., 94: 3691–3905.

Lavenu, A., 1986. Etude néotectonique de l'Altiplano et de la Cordillère Orientale des Andes Boliviennes. Thèse Doc. Etat, Univ. Orsay, 433 pp.

Lehmann, B., 1978. A Precambrian core sample from the Altiplano/Bolivia. Geol. Rundsch., 67: 270–278.

Martinez, C., 1980. Structure et évolution de la chaîne Hercynlenne et de la chaîne Andine dans le nord de la cordillère des Andes de Bolivie. Trav. Doc. ORSTOM, 119, 351 pp.

Martinez, C. and Seguret, M., 1990. Les bassins tertiaires de l'Altiplano sont-ils des bassins flexuraux intrachaine? Symp. Int. "Géodynamique Andine", ORSTOM, pp. 277–280.

Meissner, R., 1986. The Continental Crust, a Geophysical Approach. Int. Geophys. Ser. 34, 426 pp.

Meyer, H.C. and Murillo, F.J.E., 1961. Sobre la geologia en las provincias Aroma, Pacajes y Carangas. Bol. Dep. Nac. Geol. 1.

Ocola, L.C., Meyer, R.P. and Aldrich, L.T., 1971. Gross crustal structure under Peru–Bolivia Altiplano. Earthquakes Notes, 42(3–4): 33–48.

Pavlis, G.L. and Booker, J.R., 1980. The mixed discrete continuous inverse problem: Application to the simultaneous determination of earthquake hypocenters and velocity structure. J. Geophys. Res., 85: 4801–4810.

Rivera, L. and Cisternas, A., 1990. Stress tensor ad faalt plane solutions for a population of earthquakes. Bull. Seismol. Soc. Am., 80: 600–614.

Randall, M.J., 1971. A revised travel-time table for S. Geophys. J. R. Astron. Soc., 22: 229–234.

Roeder, D., 1988. Andean-age structure of Eastern Cordillera (Province of La Paz, Bolivia). Tectonics, 1: 23–39.

Sempere, T., Herail, G., Oller, J. and Bonhomme, M.G., 1990. Late Oligocene–early Miocene major tectonic crisis and related basins in Bolivia. Geology, 18: 946–949.

Sacks, I.S., 1977. Interrelationships between volcanism, seismicity and anelasticity in western south America. Tectonophysics, 37: 131–139.

Strunk, S., 1990. Analyse und Interpretation des Schwerefeldes des aktiven Kontinenralrandes des zentralen Anden (20°–26° S). Berl. Geowiss. Abh. B 17, 135 pp.

Thurber, C.H., 1983. Earthquake locations and three-dimensional crustal structure in the Coyote Lake area, central California. J. Geophys. Res., 88: 8226–8236.

Wigger, P., 1988. Seismicity and crustal structure of the central Andes. In: H. Bahiburg, Ch. Breitkreuz and P. Giese (Editors), The Southern Central Andes. Lect. Notes Earth Sci., 17: 209–229.